Journal of Energy Chemistry 107 (2025) 713–721

Contents lists available at ScienceDirect

Journal of Energy Chemistry

journal homepage: www.elsevier.com/locate/jechem

http://www.journals.elsevier.com/journal-of-energy-chemistry/

Coupling macro-strain and micro-strain for high-performance PtCo fuel cell catalysts

Xiaomei Wu [a], Zhanyong Xu [a], Fujun Lan [b,c], Yuxin Liu [b], Xinlong Wang [d], Hao Wang [d], Le Wei [a], Guowei Wang [e], Chaowei Wang [a], Ge Chen [a], Yingjun Sun [d,*], Qiaoshi Zeng [b,c,*], Manling Sui [a], Xiaoxing Ke [a,*]

[a] Beijing Key Laboratory of Microstructure and Properties of Solids, College of Materials Science & Engineering, Beijing University of Technology, Beijing 100124, China
[b] Center for High Pressure Science and Technology Advanced Research, Shanghai 201203, China
[c] Shanghai Key Laboratory of Material Frontiers Research in Extreme Environments (MFree), Institute for Shanghai Advanced Research in Physical Sciences (SHARPS), Shanghai 201203, China
[d] Institute of Energy Power Innovation, North China Electric Power University, Beijing 102206, China
[e] Ordos Laboratory, Ordos 017000, Inner Mongolia, China

ARTICLE INFO

Article history:
Received 2 March 2025
Revised 7 April 2025
Accepted 7 April 2025
Available online 16 April 2025

Keywords:
Oxygen reduction reaction
PtCo catalysts
Identical-location transmission electron microscopy
Structural disorder
Chemical etching

ABSTRACT

Limited by the sluggish kinetics at the cathode of proton exchange membrane fuel cells (PEMFCs), optimizing platinum-based alloy catalysts for oxygen reduction reaction remains a key target toward industrialization. Strain engineering is widely employed to tune Pt-M catalysts, but its impact on the structure-property relationship is often interwoven with multiple factors. In this work, we propose a bi-stage strain tuning method and demonstrate it on the most common PtCo catalysts. Macro-strain is introduced by synthesizing single-crystal PtCo nanodendrites, whereas mild acid etching introduces micro-strain to the surface. The half-wave potential of as-treated catalysts reaches 0.959 V, and mass activity is up to 0.69 A mg_{Pt}^{-1}. A minimal decrease of 2 mV is observed for half-wave potential after 10,000 cycles. Detailed analysis using advanced transmission electron microscopy, wide-angle X-ray scattering, etc. provides direct evidence that surface disorder at the atomic scale accounts for the enhanced activity and stability. In contrast, the simplicity of this approach allows for scaling up on Pt-M catalysts, as demonstrated on PEMFCs. The bi-stage strain tuning strategy provides a new perspective and reference for improving the activity and durability of Pt-M catalysts.

1. Introduction

The kinetics of oxygen reduction reaction (ORR) at the cathode of proton exchange membrane fuel cells (PEMFCs) is notably sluggish, requiring catalysts development towards industrialization [1–5]. The application of platinum-transition metal (Pt-M) catalysts has effectively accelerated the process, among which platinum-cobalt (PtCo) alloy catalysts with excellent electrocatalytic activity and stability have been demonstrated to be one of the most effective catalysts for ORR [6–9]. Co can tune the electronic structure of Pt catalysts by introducing macro-strain through ligand and strain effects, thus enhancing the activity while reducing the loading of Pt [10–12]. PtCo nanoparticles with large surface areas have been reported to be employed in commercial applications such as Toyota Mirai fuel cell vehicles [13]. However, in such small nanocrystals, the crystallinity is usually low, which may undermine macro-strain. In addition, under the operating conditions of high voltage (0.6–1.0 V) and strong acidity (pH < 1) in PEMFCs, the dissolution of transition metals such as Co inevitably results in degraded activity and stability.

Acid etching is commonly employed to enhance the stability of Pt-M alloy catalysts. Hydrochloric acid, nitric acid, sulfuric acid, perchloric acid, acetic acid, etc. are typically selected as etching

* Corresponding authors.
E-mail addresses: sunyj@ncepu.edu.cn (Y. Sun), zengqs@hpstar.ac.cn (Q. Zeng), kexiaoxing@bjut.edu.cn (X. Ke).

https://doi.org/10.1016/j.jechem.2025.04.007

agents to de-alloy M from Pt-M [14–18]. On the one hand, the surface of the catalysts becomes rough and high-index crystallographic facets are exposed, leading to a lower coordination number and facilitating the interaction with oxygen intermediates on the catalysts, thus improving the catalytic activity [10]. On the other hand, the decrease of M content leads to the formation of Pt-rich or core-shell structures, which suppress the dissolution and improve the stability [19–21]. More recently, surface structural disorder has been introduced as a descriptor of ORR, which introduces micro-strain [22]. The disordered surfaces are present by defects, including atomic vacancies, step atoms, and grain boundaries, which serve as active sites [23–25]. Using PtNi as model catalysts, Chattot et al. [26,27] studied the surface disorder and micro-strain using wide-angle X-ray scattering (WAXS) measurements and CO_{ads} stripping measurements, and more work has followed the concept. However, direct evidence of surface disorder at the atomic scale is yet absent, and it remains unclear to what extent the micro-strain is influenced by post-treatment such as acid etching, and how it can be managed to improve electrocatalytic performance.

In this work, hydrochloric acid-etched PtCo nanodendrites (H-PtCo NDs) with ultra-high activity and stability were obtained by a simple oil bath followed by an acid etching strategy. The as-synthesized PtCo NDs exhibited a single-crystal structure with three-dimensional (3D) coral morphology, and the acid etching resulted in a unique surface with structural disorder. The single-crystal nanostructure retains macro-strain, whereas the structural disorder introduces micro-strain, which is beneficial for the adsorption of oxygen intermediates and thus improves ORR. H-PtCo NDs were demonstrated to have an optimal binding energy for oxygen intermediates with half-wave potential ($E_{1/2}$) of up to 0.959 V and mass activity (MA) of up to 0.69 A mg_{Pt}^{-1}, which were significantly higher than those achieved by commercial Pt/C catalysts and as-reported PtCo NDs. H-PtCo NDs also exhibited excellent stability after cycling for 10,000 (10k) cycles with only 2 mV of loss in $E_{1/2}$. Direct evidence of surface disorder is given at the atomic scale using a novel imaging technique by transmission electron microscopy, which provides additional insights into the formation of surface disorder, whereas its impact on the electrocatalytic performance is discussed.

2. Experimental

2.1. Synthesis of PtCo NDs/C nanocatalysts

The PtCo nanodendrites were prepared via a facile oil-bath method. In a typical synthesis, 16 mg of $Pt(acac)_2$, 14 mg of $Co(acac)_3$, 160 mg of cetyltrimethylammonium chloride ($C_{19}H_{42}NCl$, CTAC), 242 mg of 1-nitroso-2-naphthol (1-N-2-N), and 15 mg of carbon black (Vulcan XC-72) were added to a glass vial containing 20 mL of oleylamine (OAM). The mixed solution was sonicated for 1 h before being transferred to an oil bath at 180 °C for 12 h. The obtained PtCo nanodendrites supported on the carbon were washed three times by centrifugation at 8000 r min^{-1} through a mixture of ethanol and cyclohexane. The obtained PtCo nanodendrites are defined as PtCo NDs.

2.2. Acid etching of PtCo NDs/C nanocatalysts

The prepared PtCo NDs/C were soaked in the HCl solution, then washed by centrifugation with deionized water, and dried to finally obtain the acid-etched samples (H-PtCo NDs/C). The concentration of HCl solution, etching time, and etching temperature were determined by orthogonal experimental, as shown in Table S1.

2.3. Characterization

The components of the catalysts were identified by the inductively coupled plasma atomic emission spectrometry (Optima 8300/PerkinElmer-ICP-AES). The surface chemistry of the catalysts was determined by X-ray photoelectron spectroscopy (XPS, Al K_α). Raman spectra were acquired by a Laser Micro Confocal Raman Spectrometer-B421. The wettability of the catalysts was determined by a Contact Angle Analyzer-C440 (Dataphysics-TP50). High angle annular dark field scanning transmission electron microscopy (HAADF-STEM), energy dispersive X-ray spectroscopy (EDS), selected area electron diffraction (SAED), and bright field high-resolution transmission electron microscopy (HRTEM) were conducted on a FEI Titan G2 microscope equipped with an aberration corrector for probe-forming lens and a Bruker Super-X EDS detector operated at 300 kV. The secondary electron STEM imaging (SE-STEM) was acquired by JEM-ARM300F2.

The method of identical-location TEM (IL-TEM) was as follows: firstly, the catalysts dispersed in ethanol were dripped on lacey support films to obtain the morphology of the catalysts using TEM; then the lacey support film was immersed in hydrochloric acid solution, rinsed with deionized water, and dried; finally the same particles were observed using TEM.

2.4. Electrochemical measurements

All electrochemical measurements were operated in a three-electrode system on an electrochemical workstation (CHI 760E, CH Instruments). A platinum foil and saturated calomel electrode (SCE) were used as the counter electrode and the reference electrode, respectively. The working electrode was a glassy carbon rotating disk electrode (GC-RDE) with an area of 0.196 cm^2. The ink was prepared by dispersing 2 mg of powder catalysts in 0.995 mL of ethanol and 0.005 mL of 5% Nafion to load the GC with 0.04 mg cm^{-2} of Pt.

0.1 M $HClO_4$ solution was prepared as the electrolyte, and saturated N_2 or O_2 was introduced for different tests. Firstly, the working electrode was electrochemically activated for 100 cycles at 100 mV s^{-1} in N_2-saturated solution. Then, the cyclic voltammetry (CV) curves were similarly recorded in the above system at 50 mV s^{-1}. The linear sweep voltammetry (LSV) curves were plotted at a scan rate of 20 mV s^{-1}, and the rotation speed was 1600 r min^{-1} with a 95% of *iR* compensation. For the accelerated durability tests (ADT), the CV curves and LSV curves were obtained by sweeping 10,000 (10k) cycles at 0.6–1.0 V vs. reversible hydrogen electrode (RHE).

The electrochemical active surface area (ECSA) was calculated by integrating the areas of hydrogen (H) absorption between 0.05 and 0.40 V_{RHE} after the deduction of the double-layer region. The ECSA value can be calculated by the following Eq. (1).

$$\mathrm{ECSA} = \frac{Q_H}{m \times 2.1} \tag{1}$$

Where Q_H represents the charge for H absorption (C m^{-2}), m represents the loading of Pt (g m^{-2}) on the working electrode, and 2.1 C m^{-2} is the charge required to absorb a monolayer of H_2 on the clean Pt.

The kinetic current density (i_k) was calculated according to the following Koutecky-Levich Eq. (2).

$$i_k = \frac{i_{0.9} \times i_{lim}}{i_{0.9} - i_{lim}} \tag{2}$$

Where $i_{0.9}$ denotes the current density at 0.9 V_{RHE} and i_{lim} denotes the diffusion-limited current density obtained from LSV curves. Further calculations determine the kinetic current per unit active area and the kinetic current per unit mass of Pt.

2.5. CO_{ads} stripping measurements

A monolayer of CO_{ads} was adsorbed on the surface of the catalysts by introducing CO gas into the electrolyte for 6 min at an electrode potential of E = 0.1 V_{RHE}. Then, it was purged with Ar at the same potential for 20 min. Finally, to strip off the CO_{ads} layer, the 3 cycles of voltammetry at 0.05–1.23 V vs. RHE were recorded at 20 mV s^{-1}.

2.6. Wide-angle X-ray scattering (WAXS) measurements

WAXS experiments were conducted using an X-ray source (MetalJet E1 + 160 kV) with an In-Ga target. The X-ray wavelength was 0.5124 Å, and the beam size was ~100 × 100 μm^2. The exposure time was 600 s. The diffractometer setup was calibrated using CeO_2 powder as the standard. Two-dimensional diffraction images were captured using a photon-counting pixel array detector (PILATUS R CdTe 1 M) and subsequently integrated into one-dimensional XRD patterns using the software Dioptas.

2.7. Density functional theory (DFT)

Spin-polarized electronic structure calculations were performed using the plane-wave basis set approach as implemented in the Vienna ab initio simulation package (VASP). The projector-augmented-wave (PAW) method was used to represent the ion-core electron interactions. The valence electrons were represented with a plane wave basis set with an energy cutoff of 450 eV. Electronic exchange and correlation were described with the Perdew-Burke-Ernzerhof (PBE) functional. DFT-D3 method was used to treat the van der Waals interaction. 15 Å of vacuum space was included to avoid interactions between surface slabs. A 3 × 3 × 1 Monkhorst-Pack scheme was used to generate the k-point grid for the modeled surfaces. The convergence criteria for the self-consistent electronic structure and geometry were set to 10^{-5} eV and 0.05 eV $Å^{-1}$, respectively.

3. Results and discussion

3.1. Promoting electrochemical performance by simple acid etching

A simple oil-bath method was used to prepare PtCo NDs with dendritic morphology and uniform size of around 49 nm. H-PtCo NDs were further obtained by hydrochloric acid etching, as shown in Figs. S1 and S2. To evaluate the effect of acid etching on the performance of PtCo NDs, orthogonal experiments were conducted to optimize etching conditions, as summarized in Table S1, Figs. S3 and S4. The optimal condition was then determined to be 0.5 M HCl for 3 h at room temperature.

The catalytic activity for PtCo NDs, H-PtCo NDs, and commercial Pt/C catalysts was evaluated and compared as shown in Fig. 1 and Fig. S5. As depicted in the CV curves of Fig. S5(a), the peaks of hydrogen (H) absorption/desorption occurring at 0.05–0.40 V vs. RHE are attributed to the presence of Pt, indicating that Pt in the catalysts is exposed and contributes to the activity [28,29]. In the interpretation of CV curves of Pt nanoparticles, {110} facets correspond to 0.10 V, {111} facets correspond to 0.18 V, and {100} facets correspond to 0.23 V [30]. In the CV curves of Pt/C catalysts, broad peaks vaguely corresponding to {110} and {111} facets can be observed. In contrast, three distinctive peaks corresponding to all three facets can be noticed in the CV curves of PtCo NDs and particularly H-PtCo NDs (enlarged in Fig. 1a). The sharper peaks of H-PtCo NDs indicate that more Pt is exposed on the surface and near-surface, which may be due to the likely formation of a Pt-rich de-alloyed surface after the removal of Co by acid etching. The two peaks appearing between 0.60 and 1.00 V_{RHE} represent the absorption/desorption peaks of oxygen and the oxygen-containing intermediates (OH_{ads}), whose adsorption/desorption rate is decisive to the ORR speed of Pt-based catalysts. Fig. 1(b) provides a detailed view of the oxygen desorption peak from the CV curves in Fig. S5(a). Compared to the Pt/C catalysts, PtCo NDs demonstrate a more positive and H-PtCo NDs demonstrate a less positive reduction potential for OH_{ads}. It has been reported that [31], a higher reduction potential corresponds to a weaker chemisorption strength of OH_{ads}. Hence, the chemisorption strength of OH_{ads} on the catalysts follows the order of PtCo NDs < H-PtCo NDs < Pt/C catalysts. According to the d-band center theory, the weakening chemisorption of OH_{ads} can be attributed to the downward shift of the d-band center relative to the Fermi energy level [32]. Thus, it is plausible that H-PtCo NDs possess a d-band center located between that of Pt/C and PtCo NDs. Notably, a new peak between 0.30 and 0.40 V_{RHE} is present in H-PtCo NDs shown in Fig. 1(a) (purple arrow), indicating partial replacement of H_{ads} by OH_{ads}. The reaction is Pt-H_{ads} + H_2O ↔ Pt-OH_{ads} + $2H^+$ + $2e^-$, which usually occurs at the terraced steps or kinks of the surface [33].

Starting from the H adsorption peak in the CV curves, the ECSA of the catalysts was calculated, as displayed in Fig. 1(c). ECSA is 76.51 m^2 g_{Pt}^{-1} for Pt/C catalysts and 36.55 m^2 g_{Pt}^{-1} for PtCo NDs, whereas H-PtCo NDs exhibit the ECSA value of 57.82 m^2 g_{Pt}^{-1}, mainly attributed to the increase of active sites by acid etching.

In addition, we evaluated the effect of etching on carbon support and its impact on ORR performance by double-layer capacitance parameter (C_{dl}), TEM imaging, XPS, Raman spectroscopy, and contact angle measurements. As obtained from the double-layer region of the CV curves, the C_{dl} of PtCo NDs and H-PtCo NDs exhibits minimal change, revealing that the acid etching has negligible impact on the conductivity of the carbon support. Detailed characterizations of the carbon support before and after acid etching were carried out, as shown in Fig. S6. Both XPS and Raman spectroscopy show negligible difference (Fig. S6a and b). Identical-location TEM (IL-TEM) (see details in Section 2.3) compares the same region of carbon support before and after etching (Fig. S6c–j), which also shows little change but only trivial roughening of the surface, consistent with literature [34]. Since proper hydrophobicity can avoid water flooding during the catalytic reactions [35], the change in wettability due to the roughness of the carbon support was analyzed by employing a contact angle test (Fig. S6k–r). Nevertheless, in the presence of Nafion, PtCo NDs and H-PtCo NDs again show negligible differences; therefore, the impact of acid etching on carbon support can be excluded.

ORR performance of as-studied catalysts was further measured by LSV curves recorded in a 0.1 M $HClO_4$ at 1600 r min^{-1} and a scan rate of 20 mV s^{-1}. As shown in Fig. 1(d), the half-wave potential ($E_{1/2}$) of H-PtCo NDs reaches 0.959 V, which is 71 mV higher than that of Pt/C catalysts (0.888 V) and 42 mV higher than that of PtCo NDs (0.917 V). The nanodendrites exhibit excellent catalytic activity compared to Pt/C catalysts, both before and after acid etching. The specific activity (SA) and mass activity (MA) at 0.9 V_{RHE} are evaluated and plotted in Fig. 1(e). H-PtCo NDs exhibit the optimal ORR activity with SA of 1.19 mA cm_{Pt}^{-2} and MA of 0.69 A mg_{Pt}^{-1}, which are 1.8 and 2.9 times higher than those of PtCo NDs, and 8.5 and 6.3 times higher than those of Pt/C, respectively, far exceeding benchmarked MA of 0.44 A mg_{Pt}^{-1} set by the U.S. Department of Energy (DOE) for 2025 [36,37]. Turnover frequency (TOF) for Pt/C, PtCo NDs, and H-PtCo NDs were further calculated. As shown in Fig. 1 (f), Pt/C has the lowest TOF value, while the TOF values of PtCo NDs and H-PtCo NDs increased by 1.2 and 2.8 times, respectively. The maximum TOF value of H-PtCo NDs indicates the best intrinsic activity.

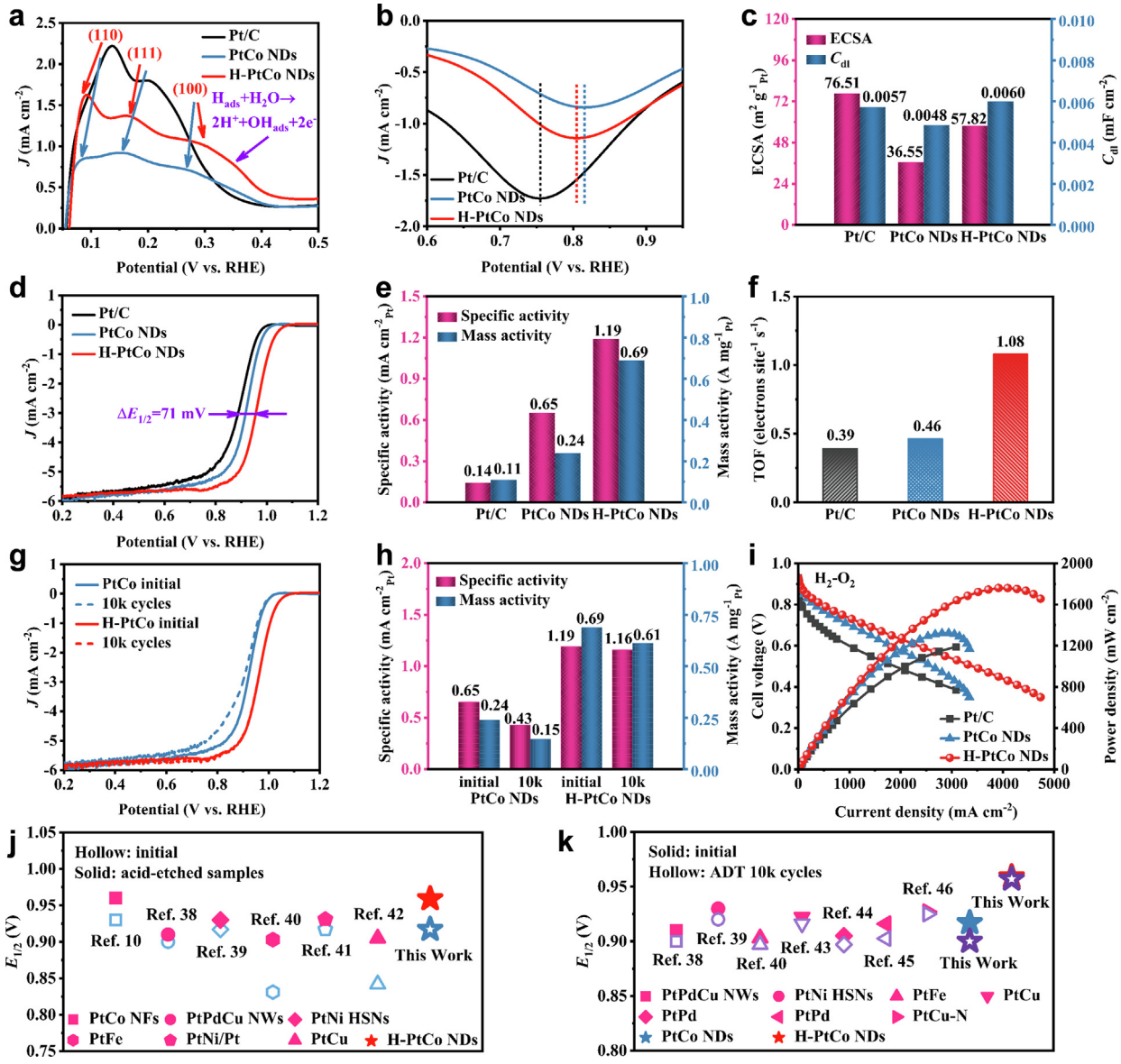

Fig. 1. ORR performance of commercial Pt/C, PtCo NDs, and H-PtCo NDs catalysts. (a) Magnified plots of H desorption peak in the CV curves; (b) magnified plots of O desorption peak in the CV curves; (c) the ECSA and the double-layer capacitance parameter (C_{dl}); (d) LSV curves; (e) the specific activity and mass activity of three catalysts; (f) TOF; (g) LSV curves before and after ADT-10k; (h) specific activity and mass activity before and after ADT-10k; (i) polarization and power density curves in H_2-O_2 fuel cells; (j) the half-wave potential ($E_{1/2}$) of different catalysts before and after acid etching [10,38–42]; (k) $E_{1/2}$ of different catalysts before and after ADT-10k [38–40,43–46].

The stability of the catalysts was evaluated by ADT after sweeping 10,000 (10k) cycles in the potential range of 0.6–1.0 V_{RHE}. The CV and LSV curves are plotted in Fig. S5(b) and Fig. 1(g), respectively. Compared to the negative shift of PtCo NDs catalysts, LSV curves show that H-PtCo NDs maintain the initial ORR polarization curves after 10k cycles, thus demonstrating excellent stability, with $E_{1/2}$ decreasing by only 2 mV and SA and MA decreasing by only 2.5% and 11.6% (Fig. 1h). The excellent stability of H-PtCo NDs can also be demonstrated by the ICP results in Table S2.

The PEMFC performance of Pt/C, PtCo NDs, and H-PtCo NDs was evaluated in a hydrogen fuel cell under H_2-O_2 and H_2-air using an anode loading of 0.05 mg_{Pt} cm^{-2} for 40 wt% Pt/C and a cathode loading of 0.1 mg_{Pt} cm^{-2} for three catalysts. In H_2-O_2 conditions, as displayed in Fig. 1(i), H-PtCo NDs and PtCo NDs achieve the peak power density of 1.76 and 1.32 W cm^{-2}, respectively, comparable to commercial Pt/C (1.19 W cm^{-2}). While under H_2-air conditions, as displayed in Fig. S5(c), H-PtCo NDs afford higher current density than PtCo NDs and Pt/C, indicating its excellent intrinsic activity. Hence, H-PtCo NDs exhibit great potential as cathode catalysts for PEMFCs. Fig. 1(j) and Table S3 compared the $E_{1/2}$ of PtCo NDs and H-PtCo NDs with similar acid-treated Pt-based nanocatalysts recently reported in the literature [10,38–42]. Fig. 1(k), Tables S3 and S4 further compared the $E_{1/2}$ of these catalysts before and after 10k cycles [38–40,43–46]. In addition, Table S5 compared the ORR performance of PtCo catalysts for the last three years. Our H-PtCo NDs have both excellent ORR activity and stability, outperforming most PtCo catalysts reported to date.

3.2. Surface chemical structure modification by acid etching

Significant improvement of ORR performance after acid etching should be related to the structural change of either PtCo NDs or carbon support. Previous investigation showed little change in the carbon support. Hence, detailed structural characterization on PtCo NDs was conducted as shown in Fig. 2. The morphology and crystal structure of PtCo NDs and H-PtCo NDs

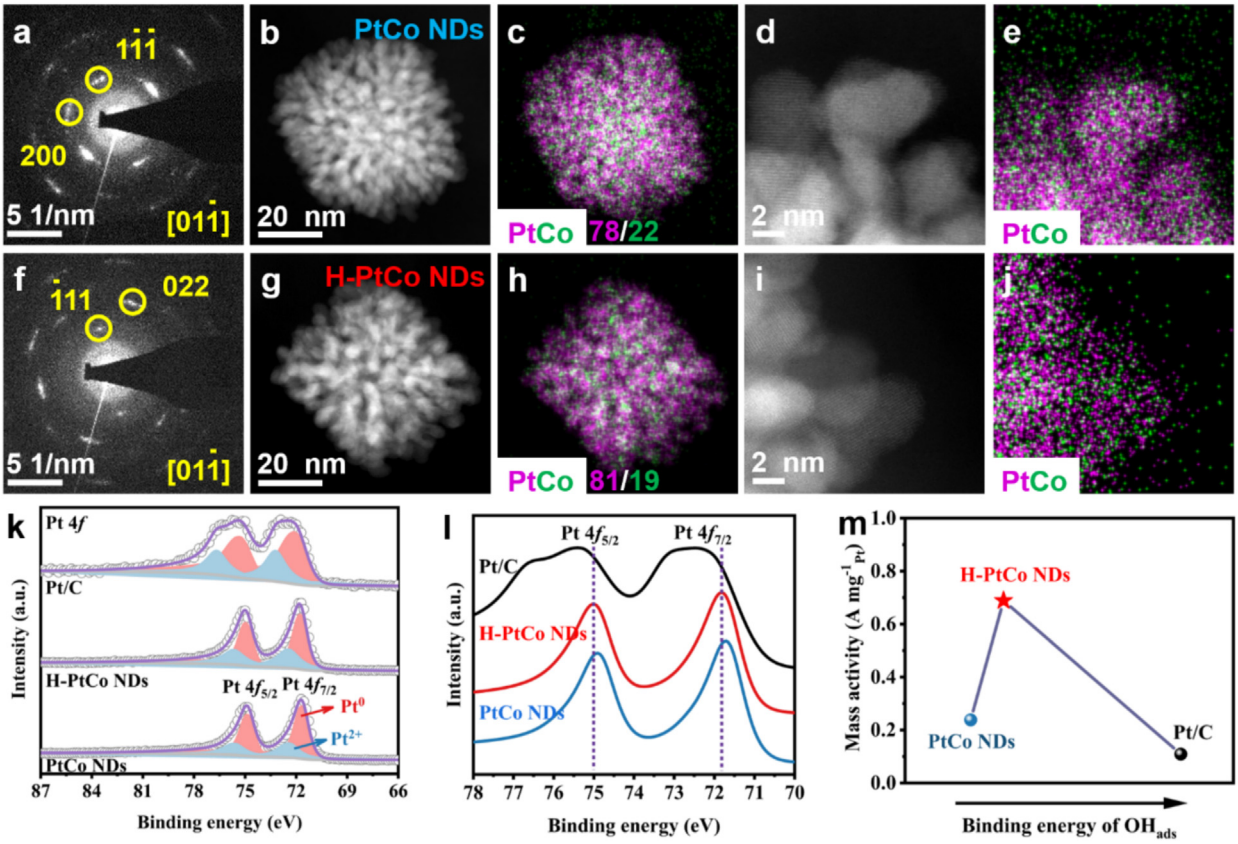

Fig. 2. Structural characterization of Pt/C, PtCo NDs, and H-PtCo NDs catalysts. SAED of (a) PtCo NDs and (f) H-PtCo NDs; HAADF-STEM images of (b) PtCo NDs and (g) H-PtCo NDs at low magnification; (c, h) corresponding EDS mappings of (b and g); HAADF-STEM images of (d) PtCo NDs and (i) H-PtCo NDs at high magnification; (e, j) corresponding EDS mappings of (d and i); (k) XPS spectra of Pt 4*f*; (l) enlargement of (k); (m) MA as a function of OH_{ads} binding energy.

were characterized from the SAED, HAADF-STEM, EDS, and XPS. SAED patterns of an isolated PtCo ND (Fig. 2a) and an isolated H-PtCo ND (Fig. 2f) show that both nanodendrites exhibit a single-crystalline-like structure, which can be indexed to zone axes of [01 $\bar{1}$] following the face-center cubic (FCC) structure. In the single-crystal structure, the macro-strain due to the alloying of Pt with Co is well maintained in the nanodendrites. After acid etching, the diffraction spots are not as sharp but elongated to streaks, originating from rotations of small crystal domains, implying the presence of defects and the introduction of micro-strain. The dendritic morphologies of PtCo NDs and H-PtCo NDs were characterized by HAADF-STEM (Fig. 2b, g), showing no distinct difference.

Meanwhile, the EDS mappings (Fig. 2c, h) show that Pt and Co are homogeneously distributed throughout the nanodendrites both in PtCo NDs and H-PtCo NDs. However, the atomic ratio of Pt to Co increases from 78/22 (3.5/1) to 81/19 (4.3/1), revealing the heavier loss of Co compared to Pt by acid etching. Since most reported work claimed that the dissolution of transition metal led to the formation of Pt shell after acid etching [20,47], we used EDS mappings at higher magnification to study the surface composition as shown in Fig. 2(d, e, i, j), and Fig. S7(a, b, e, f). However, Pt shell is not obvious in our work, which could be explained as follows. HAADF-STEM is a *Z*-contrast imaging technique, where the intensity scales with *Z*-number; as-synthesized PtCo contains a low amount of Co and average *Z* is close to Pt; hence, the loss of Co from the surface can hardly be reflected as a sharp change of *Z* value. Additionally, we characterized the catalysts after electrochemical cycling, but no distinguishable Pt shell is found either, as shown in Figs. S7(c, d, g, h) and Fig. S8.

The surface electronic properties and valence states of the catalysts were examined through XPS as shown in Fig. 2(k). In the Pt 4*f* spectra, all catalysts exhibit two characteristic peaks as Pt $4f_{7/2}$ (71.7 eV) and Pt $4f_{5/2}$ (75.0 eV), each of which can be deconvoluted into a double peak of Pt^0 and Pt^{2+}, where the presence of Pt^{2+} may be due to the oxidation by air. Compared to the Pt/C catalysts, the Pt 4*f* peaks of PtCo NDs and H-PtCo NDs negatively shift, indicating a weakened adsorption strength with ORR intermediates relative to Pt/C. Further comparison reveals that the Pt 4*f* peaks of H-PtCo NDs are located between those of Pt/C and PtCo NDs, as shown in Fig. 2(l), indicating that the adsorption strength of the catalysts for OH_{ads} is also in between, which verifies the speculative results from CV curves (O desorption peak in the CV curves in Fig. 1b). MA and SA, as functions of the binding energy of the catalyst to OH_{ads}, respectively, exhibit volcano shaped plots [31,48,49], as shown in Fig. 2(m) and Fig. S9. H-PtCo NDs are located at the top of the volcano, where the optimized binding energy for OH_{ads} maximizes ORR activity, following the Sabatier principle.

3.3. Direct evidence of surface disorder introduced by acid etching

Although significant improvement of ORR performance by acid etching has been confirmed, morphological evidence is yet absent, whereas neither carbon support nor Pt shell on H-PtCo NDs was noticed. Hence, we focused on the surface structure of PtCo at the atomic scale using WAXS measurement and IL-TEM.

WAXS patterns in reciprocal space of PtCo NDs and H-PtCo NDs are shown in Fig. S10(a). Both PtCo NDs and H-PtCo NDs exhibit FCC structure. The WAXS patterns are shown in Fig. 3(a). Notably,

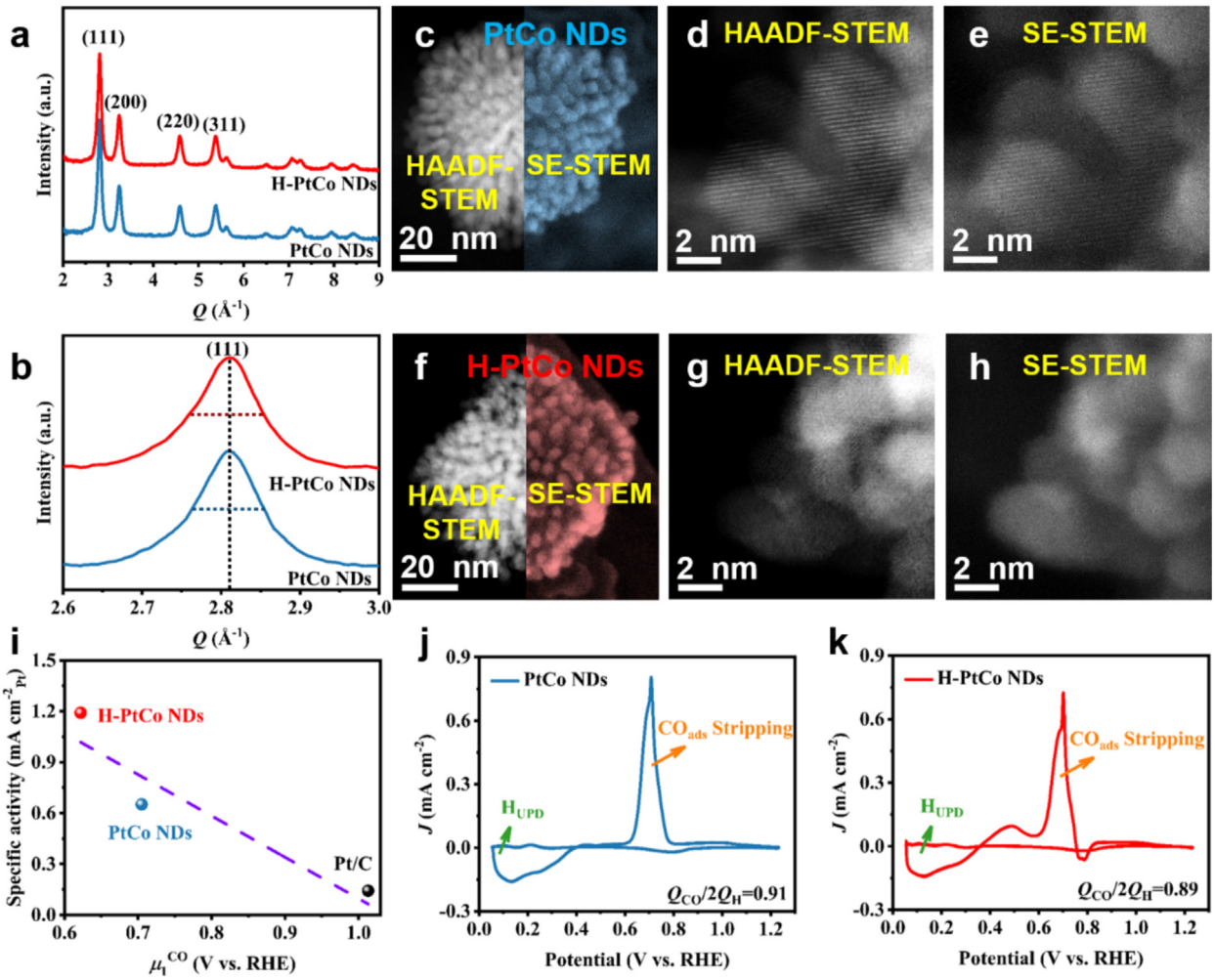

Fig. 3. Structural disorder characterization of Pt/C, PtCo NDs, and H-PtCo NDs catalysts. (a) WAXS patterns; (b) magnified (111) peaks of PtCo NDs and H-PtCo NDs catalysts; (c, f) HAADF-STEM images (left) and SE-STEM images (right) of PtCo NDs and H-PtCo NDs catalysts at low magnification; (d, g) HAADF-STEM images at high magnification; (e, h) SE-STEM images at high magnification; (i) relationships between the SA at 0.90 V_{RHE} and the average oxidation potential μ_1^{CO}; (j) background-subtracted CO_{ads} stripping voltammograms of PtCo NDs; (k) background-subtracted CO_{ads} stripping voltammograms of H-PtCo NDs.

the first WAXS peak of the H-PtCo NDs displays a slight broadening (measured to be 5.78%) compared to the PtCo NDs, as shown in Fig. 3(b), suggesting enhanced structural disorder, which can induce micro-strain on the surface of catalysts. The WAXS data were further analyzed in real space by Fourier transform reduced by pair distribution function (PDF) as shown in Fig. S10(b and c). Compared to PtCo NDs, H-PtCo NDs show lower peak intensity in $G(r)$, e.g., a 2.18% decrease in the peak intensity of the Pt–Co first coordination shell between 2.2 and 3.3 Å, which also suggests enhanced structural disorder.

Direct evidence of surface disorder is given by TEM investigation using novel SE-STEM imaging. SE-STEM in TEM detects secondary electrons, which is sensitive to surface structures, therefore reflecting the surface atomic structure instead of bulk structure as in conventional TEM imaging [50,51]. Fig. 3(c–h) displays HAADF-STEM and SE-STEM images of PtCo NDs before and after etching. Low-magnification STEM images of an isolated PtCo ND and an isolated H-PtCo ND combining HAADF detector and SE detector are shown in Fig. 3(c and f). Compared to conventional HAADF-STEM images, SE-STEM images display the 3D topology of the nanodendrites, although little difference can be noticed at this magnification. Atomically resolved HAADF-STEM images (Fig. 3d, g) and SE-STEM images (Fig. 3e, h) before and after acid etching are further compared. For PtCo NDs, both HAADF-STEM and SE-STEM images match well and show lattice fringes, implying that their surface atomic structure is the same as the bulk structure. However, for H-PtCo NDs, the simultaneously acquired HAADF-STEM image (Fig. 3g) and SE-STEM image (Fig. 3h) show completely different contrast. The HAADF-STEM image representing the crystallinity along the viewing direction remains lattice structure, but the SE-STEM image (Fig. 3h) hardly shows any fringes but only amorphous-like topology. These results obtained by STEM imaging at the atomic scale are consistent with WAXS on powder samples, supporting our scenario that the surface atomic coordination environment is disrupted as well as the presence of localized surface defects is introduced by acid etching.

The impact of the surface disorder on catalytic activity is also supported by CO_{ads} stripping voltammograms. Due to the high sensitivity, microstructural changes in the catalysts can be recognized by the number, location, and shape of the CO_{ads} stripping peaks [52]. After acid etching, H-PtCo NDs show a slightly negative shift at 0.60–0.80 V_{RHE} and an additional peak at 0.40–0.60 V_{RHE}, as shown in Fig. S11(b). For quantitative comparison, the average oxidation potential μ_1^{CO} (V_{RHE}) of CO_{ads} is calculated and plotted against SA as shown in Fig. 3(i). It can be found that H-PtCo NDs with higher surface disorder have the lowest μ_1^{CO}, indicating that

the catalyst tends to adsorb water and dissociate to *OH, which promotes the oxidation of CO. The same OH-generating ability also promotes O–O bond breaking during ORR, thus enhancing the reaction kinetics. Further comparison is made between the charge (Q) of the catalysts for the desorption of underpotentially deposited H (i.e. H_{UPD}) and the electrooxidation of monolayers of CO_{ads}. It has been shown that the ratio of $Q_{CO}/2Q_H$ is the fingerprint for electrochemical adsorption and is almost linear with the degree of surface disorder. A defect-free surface corresponds to $Q_{CO}/2Q_H \geq 0.94$, whereas the presence of surface disorder lowers the ratio to 0.75–0.92 [33]. The values of $Q_{CO}/2Q_H$ of PtCo NDs and H-PtCo NDs catalysts are then calculated, as shown in Fig. 3(j) (Fig. S11c) and Fig. 3(k) (Fig. S11d). The ratio of $Q_{CO}/2Q_H$ of PtCo NDs is 0.91, and that of H-PtCo NDs is 0.89, consistent with previous results of surface disorder introduced by acid etching.

3.4. Generation of surface disorder and micro-strain revealed at the atomic scale

We finally revealed the generation of surface disorder by acid etching using IL-TEM, where the same location of PtCo NDs before and after acid etching was compared and analyzed, as shown in Fig. 4 (see details in Section 2.3). Two randomly-chosen nanodendrites were compared before and after etching, where Fig. 4(a–j) demonstrates one nanodendrite and Fig. 4(k–t) demonstrates another. Firstly, TEM images at low magnification show that the nanodendrites remain uniformly dispersed on the carbon support before and after acid etching, and no migrations of particles are noticed, as indicated by green boxes in Fig. 4(a, f, k, p). The green boxed areas are enlarged in Fig. 4(b, g, l, q), showing that the morphology of individual nanodendrites remains unchanged. Meanwhile, corresponding SAED patterns (Fig. S12) show that the nanodendrites maintain single crystalline too.

Secondly, the protruded "branch" on the nanodendrites (Fig. 4c, h, m, r) is investigated using HRTEM (Fig. 4d, i, n, s) and aberration-corrected HAADF-STEM (Fig. S13). As-synthesized nanodendrites are dominated by smooth {111} and {100} facets, and acid etching generates terraced steps on the facets. By comparing the same "branch" before and after etching at the atomic scale, the generation of surface steps is demonstrated by atomic model diagrams in Fig. 4(u and v), respectively, where the absence of dissolved atoms is shown by blue atoms. The removal of surface atoms generates surface steps with under-coordinated atoms, which may be reconstructed in the environment of strong acidity and thus form surface disorder as revealed by SE-STEM (Fig. 3h) in a 3D manner.

In addition to the direct comparison of PtCo "nanobranch" before and after acid etching, geometric phase analysis (GPA) was applied to further quantify the distribution of micro-strain.

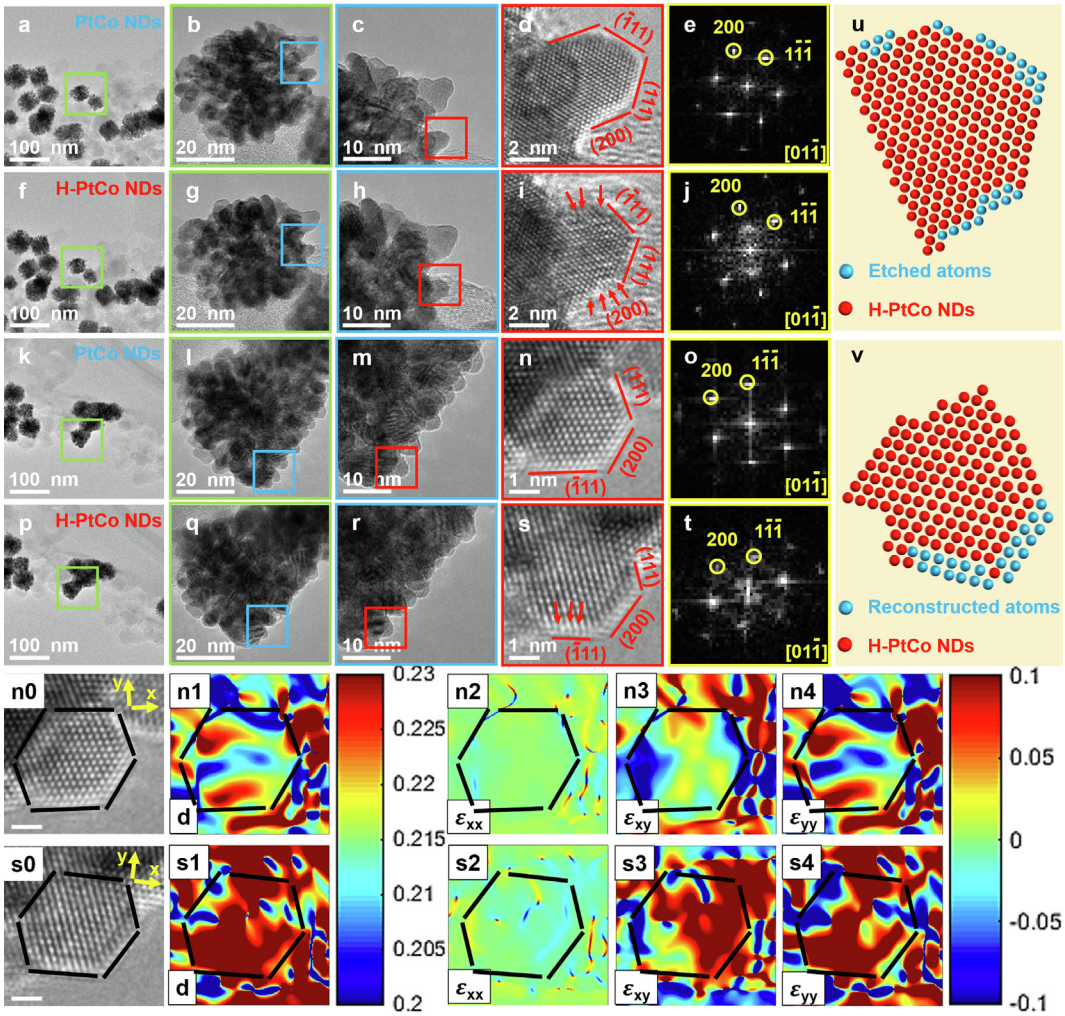

Fig. 4. The process of acid etching of PtCo NDs. TEM images and HRTEM images of (a–d, k–n) PtCo NDs and (f–i, p–s) H-PtCo NDs; FFT patterns of (e, o) PtCo NDs and (j, t) H-PtCo NDs; (u, v) model diagram of atomic etching on the surface of a single "branch" of H-PtCo NDs. HRTEM images of (n0) PtCo NDs and (s0) H-PtCo NDs; (111) *d*-spacing of (n1) PtCo NDs and (s1) H-PtCo NDs; atomic strain distribution of (n2–n4) PtCo NDs and (s2–s4) H-PtCo NDs. Black lines are projected in each figure to assist in identifying the selected PtCo and H-PtCo nanodomains.

Firstly, corresponding fast Fourier transform (FFT) patterns of both nanobranches (Fig. 4e, j, o, t) show that the "diffraction spots" become slightly diffused after acid etching, suggesting the introduction of defects. Secondly, the "nanobranch" in Fig. 4(n, s) is subjected to detailed GPA analysis as shown in Fig. 4(n0 and s0), respectively. The nanodomain for GPA analysis is outlined in black, and the detailed GPA analysis is performed with the direction of the $(\bar{1}\,11)$ facets as the *x*-axis. Compared with Fig. 4(n1), the *d*-spacing of the $(\bar{1}\,11)$ facets in Fig. 4(s1) increases from an average of 0.216 nm to as large as 0.225 nm after etching, where the red region indicates the increase in *d*-spacing. The corresponding ε_{xx}, ε_{xy}, and ε_{yy} are further shown in Fig. 4(n2–n4 and s2–s4). PtCo NDs show a uniform strain of around 0, whereas the H-PtCo NDs exhibit an increased strain, manifested by the enriched red region, especially in ε_{xy} (Fig. 4s3) and ε_{yy} (Fig. 4s4). The GPA results demonstrate that nanodendrites exhibit increased micro-strain caused by the dissolution and reconstruction of atoms after etching, which can provide a higher density of active sites on the entire surface of the catalysts, thus favoring the ORR process.'

3.5. Mechanism for improving ORR activity

Structural models of the {111} facets of Pt, PtCo NDs, and H-PtCo NDs are developed for density functional theory (DFT) calculations, as shown in Fig. 5(a–c). Fig. 5(d) shows the ORR mechanism of the H-PtCo NDs {111}, which achieves a complete four-electron transfer pathway, including: (1) $^* + O_2 + H^+ + e^- \rightarrow {}^*OOH$, (2) $^*OOH + H^+ + e^- \rightarrow {}^*O + H_2O$, (3) $^*O + H^+ + e^- \rightarrow {}^*OH$, and (4) $^*OH + H^+ + e^- \rightarrow H_2O$.

To investigate the energy barriers of these four steps, the Gibbs free energies of the Pt, PtCo NDs, and H-PtCo NDs were calculated, as shown in Fig. 5(e). The energy paths of the three catalysts at U = 0 V are similar and show spontaneous exothermic processes. However, at U = 1.23 V, three catalysts show differences. For Pt, the free energy rise in step (2) is the largest and therefore is decisive. For PtCo NDs and H-PtCo NDs, both catalysts have the largest free energy rise at step (3), indicating that the process of *O gaining electrons to combine with H^+ to form *OH, and further desorption from the catalyst surface, is the decisive step. The results demonstrate that the energy barriers of both PtCo NDs (0.85 eV) and H-PtCo NDs (0.81 eV) are smaller than that of Pt (0.91 eV), suggesting the positive effect of macro-strain due to alloying on the ORR mechanism. Meanwhile, H-PtCo NDs requires the lowest energy barrier, suggesting that it is thermodynamically favored and thus demonstrates the advantages of micro-strain.

In addition, the *d*-band center of all three catalysts was calculated as shown in the projected density of states (PDOS) in Fig. 5(f). The *d*-band center of Pt for both PtCo NDs (−2.61 eV) and H-PtCo NDs (−2.55 eV) negatively shifts compared to Pt (−2.25 eV), while H-PtCo NDs is in between. The PDOS result indicates the improvement of the adsorption energy of H-PtCo NDs with oxygen intermediates, and hence the optimization of ORR activity.

In concluion, the stability improvement of H-PtCo NDs is mainly attributed to the coupling of macro-strain (as for Pt-Co alloying effect) and micro-strain (as for surface modification by acid etching). On the one hand, the macro-strain effect and ligand effect from alloying Pt with Co dominate the ORR activity of PtCo NDs, as the entire ND is a single crystal where macro-strain is well kept. However, Co is gradually lost during the electrochemical cycling, thus weakening the strain effect and ligand effect generated by the alloying. On the other hand, acid etching introduces surface micro-strain to H-PtCo NDs, but maintains macro-strain by keeping single-crystallinity. During electrochemical cycling, the stability of H-PtCo NDs is significantly enhanced due to the dominant role of the surface micro-strain, which reduces the loss of Co and retains ORR activity.

4. Conclusions

In this work, we propose a bi-stage strain engineering approach to enhance ORR performance of PtCo. In the first stage, single-crystal PtCo NDs with three-dimensional coral-like morphology are synthesized using a simple one-step oil bath, where macro-strain is retained in the structure. Subsequent acid etching results in H-PtCo NDs with enhanced electrocatalytic performance, reaching an SA of 1.19 mA cm_{Pt}^{-2} and MA of 0.69 A mg_{Pt}^{-1}, and an excellent stability of merely 2 mV loss in $E_{1/2}$ after 10k cycles, far exceeding the DOE target in 2025. Further PEMFC results show that the power density of H-PtCo NDs reaches up to 1.76 W cm^{-2}, which is 1.5 times higher than that of Pt/C, demonstrating its potential as a cathode catalyst for PEMFCs. Detailed investigations reveal that a mild acid treatment keeps the bulk crystal intact to keep the macro-strain, but introduces micro-strain on the surface. Combining novel imag-

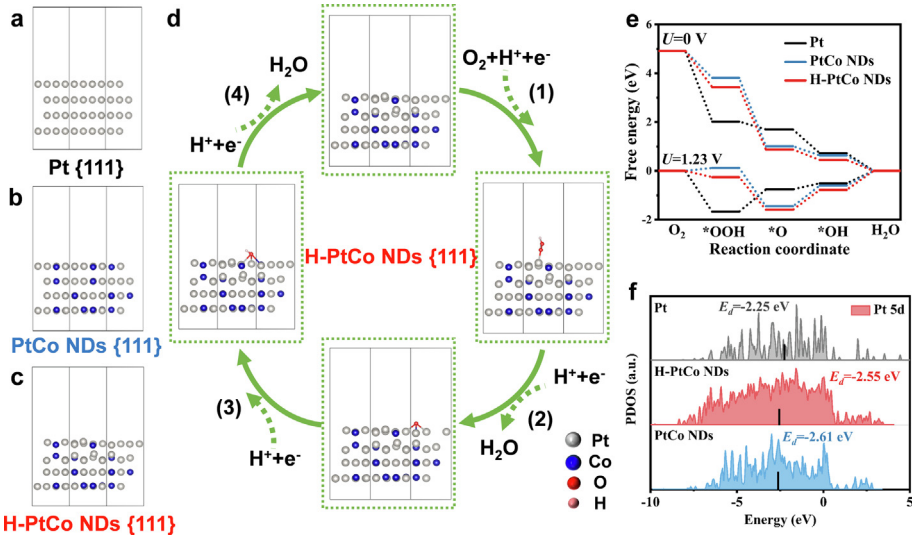

Fig. 5. DFT calculations of Pt{111}, PtCo NDs{111}, and H-PtCo NDs{111}. Structural models of the {111} facets of (a) Pt, (b) PtCo NDs, and (c) H-PtCo NDs; (d) illustration of ORR mechanism; (e) Gibbs free energy diagram at 0 and 1.23 V; (f) PDOS of the *d*-band for Pt. The black line indicates the *d*-band center.

ing techniques of SE-STEM and IL-TEM, it is revealed for the first time that an atom-thick layer of disordered surface is present and accounts for the enhanced ORR activity. Demonstrated on PtCo, which is the most common and the most promising Pt-M catalyst for commercial use, this work contributes new insights into the rational design of optimal Pt-based catalysts, allowing for scale-up using a simple approach.

CRediT authorship contribution statement

Xiaomei Wu: Writing – original draft, Visualization, Supervision, Software, Resources, Project administration, Methodology, Investigation, Formal analysis, Data curation. **Zhanyong Xu:** Methodology. **Fujun Lan:** Methodology. **Yuxin Liu:** Methodology. **Xinlong Wang:** Methodology. **Hao Wang:** Methodology. **Le Wei:** Investigation. **Guowei Wang:** Formal analysis. **Chaowei Wang:** Investigation. **Ge Chen:** Investigation. **Yingjun Sun:** Funding acquisition. **Qiaoshi Zeng:** Funding acquisition. **Manling Sui:** Investigation. **Xiaoxing Ke:** Supervision, Investigation, Funding acquisition.

Declaration of competing interest

The authors declare that they have no known competing financial interests or personal relationships that could have appeared to influence the work reported in this paper.

Acknowledgments

X.W. and X.K. acknowledge the National Natural Science Foundation of China (NO. 12274010, 12474003), and Beijing Nova Program (20240484584). Q.Z. acknowledges the support from the Shanghai Key Laboratory of Material Frontiers Research in Extreme Environments, China (No. 22dz2260800), and the Shanghai Science and Technology Committee, China (No. 22JC1410300). Y.S. acknowledges the National Natural Science Foundation of China (No. 52103330).

Appendix A. Supplementary material

Supplementary data to this article can be found online at https://doi.org/10.1016/j.jechem.2025.04.007.

References

[1] C.Y. Ahn, J.E. Park, S.J. Kim, O.H. Kim, W.C. Hwang, M. Her, S.Y. Kang, S.B. Park, O.J. Kwon, H.S. Park, Y.H. Cho, Y.E. Sung, Chem. Rev. 121 (2021) 15075–15140.
[2] J.W. Zhang, Y.L. Yuan, L. Gao, G.M. Zeng, M.F. Li, H.W. Huang, Adv. Mater. 33 (2021) 2006494.
[3] Z. Seh, J. Kibsgaard, C.F. Dickens, I. Chorkendorff, J.K. Nørskov, T. Jaramillo, Science 355 (2017) eaad4998.
[4] M.C. Luo, S.J. Guo, Nat. Rev. Mater. 2 (2017) 17059.
[5] E. Wang, L. Luo, Y. Feng, A. Wu, H. Li, X. Luo, Y. Guo, Z. Tan, F. Zhu, X. Yan, Q. Kang, Z. Zhuang, D. Yang, S. Shen, J. Zhang, J. Energy Chem. 93 (2024) 157–165.
[6] S.Y. Yu, H. Yang, Chem. Commun. (Cambridge, U.K.) 59 (2023) 4852.
[7] J.R. Li, S. Sharma, X.M. Liu, Y.T. Pan, J.S. Spendelow, M.F. Chi, Y.K. Jia, P. Zhang, D. A. Cullen, Z. Xi, H.H. Lin, Z.Y. Yin, B. Shen, M. Muzzio, C. Yu, Y.S. Kim, A.A. Peterson, K.L. More, H.Y. Zhu, S. Sun, Joule 3 (2019) 124–135.
[8] Z.X. Wang, X.Z. Yao, Y.Q. Kang, L.Q. Miao, D.S. Xia, L. Gan, Adv. Funct. Mater. 29 (2019) 1902987.
[9] L. Zhang, L. Tong, S. Li, C.S. Ma, K.Z. Xue, H.W. Liang, J. Energy Chem. 101 (2025) 1–6.
[10] M. Wei, L. Huang, L.B. Li, F. Ai, J.Z. Su, J.K. Wang, ACS Catal. 12 (2022) 6478–6485.
[11] Z.H. Xia, S.J. Guo, Chem. Soc. Rev. 48 (2019) 3265–3278.
[12] C. Li, W. Zhao, X. Lu, Z. Chen, B. Han, X. Zhang, J. Chen, Y. Shao, J. Huo, Y. Zhu, Y. Deng, S. Sun, S. Liao, J. Energy Chem. 78 (2023) 340–349.
[13] K. Kodama, T. Nagai, A. Kuwaki, R. Jinnouchi, Y. Morimoto, Nat. Nanotechnol. 16 (2021) 140–147.
[14] L. Huang, Z. Jiang, W.H. Gong, Z. Wang, P. Shen, J. Power Sources 406 (2018) 42–49.
[15] S.P. Chen, M.F. Li, M.Y. Gao, J.B. Jin, M.A. Spronsen, M.B. Salmeron, P.D. Yang, Nano Lett. 20 (2020) 1974–1979.
[16] X. Zhong, L. Wang, Z.Z. Zhuang, X.L. Chen, J. Zheng, Y.L. Zhou, G.L. Zhuang, X.N. Li, J. Wang, Adv. Mater. Interfaces 4 (2017) 1601029.
[17] B. Yang, Y.T. Zhao, L.D. Fang, Surf. Interface Anal. 52 (2020) 573–583.
[18] H. Kwon, M.K. Kabiraz, J. Park, A. Oh, H. Baik, S. Choi, K. Lee, Nano Lett. 18 (2018) 2930–2936.
[19] H.B. Tang, Y.Q. Su, B. Chi, J.W. Zhao, D. Dang, X.L. Tian, S.J. Liao, G.R. Li, Chem. Eng. J. 418 (2021) 129322.
[20] X. Lyu, Y. Jia, X. Mao, D.H. Li, G. Li, L.Z. Zhuang, X. Wang, D.J. Yang, Q. Wang, A.J. Du, X.D. Yao, Adv. Mater. 32 (2020) 2003493.
[21] H. Ding, P. Wang, C.J. Su, H.F. Liu, X.L. Tai, N. Zhang, H.F. Lv, Y. Lin, W.S. Chu, X.J. Wu, C.Z. Wu, Y. Xie, Adv. Mater. 34 (2022) 2109188.
[22] C. Raphaël, L.B. Olivier, B. Vera, S. Kühl, J. Herranz, S. Henning, L. Kühn, T. Asset, L. Guétaz, G. Renou, J. Drnec, P. Bordet, A. Pasturel, A. Eychmüller, T.J. Schmidt, P. Strasser, L. Dubau, F. Maillard, Nat. Mater. 17 (2018) 827–833.
[23] L. Dubau, J. Nelayah, T. Asset, R. Chattot, F. Maillard, ACS Catal. 7 (2017) 3072–3081.
[24] L. Dubau, J. Nelayah, S. Moldovan, O. Ersen, P. Bordet, J. Drnec, T. Asset, R. Chattot, F. Maillard, ACS Catal. 6 (2016) 4673–4684.
[25] M.H. Wu, C.L. Chen, Y.Z. Zhao, E.B. Zhu, Y.J. Li, Front. Chem. 9 (2021) 699861.
[26] C. Raphael, A. Tristan, B. Pierre, J. Drnec, L. Dubau, F. Maillard, ACS Catal. 7 (2017) 398–408.
[27] C. Raphaël, M. Isaac, S. Marion, J. Herranz, J. Drnec, F. Maillard, L. Dubau, ACS Energy Lett. 5 (2020) 162–169.
[28] H. Cui, Y.X. Chen, J. Energy Chem. 94 (2024) 70–77.
[29] R. Yang, C. Dai, L. Zhang, R. Wang, K. Yin, B. Liu, Z. Chen, J. Energy Chem. 98 (2024) 169–179.
[30] T.H. Huang, Y.J. Jiang, Y.H. Peng, Y.T. Tseng, C. Yan, P.C. Chien, K.Y. Wang, T.Y. Chen, J.H. Wang, K.W. Wang, S. Dai, ACS Appl. Mater. Interfaces 15 (2023) 18217–18228.
[31] L.M. Guo, D.F. Zhang, L. Guo, Adv. Funct. Mater. 30 (2020) 2001575.
[32] M.K. Kabiraz, B. Ruqia, J. Kim, H. Kim, H.J. Kim, Y. Hong, M.J. Kim, Y.K. Kim, C. Kim, W. Lee, G.H. Hwang, H.C. Ri, H. Baik, H. Oh, Y.W. Lee, L. Gao, H. Huang, S. M. Paek, Y.J. Jo, C.H. Choi, S.W. Han, S. Choi, ACS Catal. 12 (2022) 3516–3523.
[33] R. Chattot, I. Martens, M. Scohy, H. Juan, D. Jakub, M. Frédéric, D. Laetitia, ACS Energy Lett. 5 (2020) 162–169.
[34] H. Hu, Y. Liu, F. Shi, P. Tao, C. Song, W. Shang, X. Ke, T. Deng, X. Zeng, J. Wu, Nano Lett. 24 (2024) 2157–2164.
[35] S.N. Hu, W.C. Xu, N. Tian, S.M. Chen, M.Y. Li, J.F. Shen, J.X. Lin, S.L. Guo, X.Y. Huang, Z.Y. Zhou, S.G. Sun, Energy Environ. Sci. 17 (2024) 3099–3111.
[36] H.Y. Lee, T.H. Yu, C.H. Shin, A. Fortunelli, S.G. Ji, Y.J. Kim, T.H. Kang, B.J. Lee, B.V. Merinov, W.A. Goddard III, C.H. Choi, J.S. Yu, Appl. Catal. B Environ. 323 (2023) 122179.
[37] M.Z. Zhu, H.J. Zhang, Y.M. Hu, F.Y. Zhou, X.P. Gao, D.Y. He, X.Y. Zhao, C. Zhao, J. Wang, W.A. Tie, X.Y. Tian, B. Wang, T. Yao, H. Zhou, Z. Wang, J. Wang, W.X. Guo, Y.E. Wu, ACS Catal. 14 (2024) 5858–5867.
[38] K.L. Wang, F. Wang, Y.F. Zhao, W. Zhang, J. Energy Chem. 52 (2021) 251–261.
[39] S.B. Li, Z.Q. Tian, Y. Liu, Z. Jang, S.W. Hasan, X. Chen, T. Panagiotis, K.S. Pei, Chin. J. Catal. 42 (2021) 648–657.
[40] L.Y. Gong, J. Liu, Y. Li, X. Wang, E. Luo, J. Zhao, J. Ge, C. Liu, W. Xing, Chem. Eng. J. 428 (2022) 131569.
[41] J.Y. Jung, D.G. Kim, I. Jang, N.D. Kim, J.Y. Sung, K. Pil, J. Ind. Eng. Chem. 111 (2022) 300–307.
[42] H. Wu, H.C. Zhong, Y.Z. Pan, H. Li, Y. Peng, L. Yang, S. Luo, B. Dustin, J. Zeng, Colloid. Surf. A 656 (2023) 130341.
[43] J. Park, M.K. Kabiraz, H. Kwon, P. Suhyun, B. Hionsuck, C. Sang-Il, L. Kwangyeol, ACS Nano 11 (2017) 10844–10851.
[44] X.L. Xiong, W.L. Chen, W. Wang, Int. J. Hydrogen Energy 42 (2017) 25234–25243.
[45] R.F. Wu, Y.J. Li, W.H. Gong, K.S. Pei, ACS Sustain. Chem. Eng. 7 (2019) 8419–8428.
[46] T.S. Song, H. Xue, N.K. Guo, J. Sun, L. Qin, L. Guo, K.K. Huang, F. He, W. Qin, Chem. Commun. 56 (2020) 7136.
[47] Y. Shi, W. Yang, W. Gong, X. Wang, Y. Zhou, X. Shen, Y. Wu, J. Di, D. Zhang, Q. Li, J. Mater. Chem. A 9 (2021) 12845–12852.
[48] Y. Zheng, A.S. Petersen, H. Wan, R. Hübner, J. Zhang, J. Wang, H. Qi, Y. Ye, C. Liang, J. Yang, Z. Cui, Y. Meng, Z. Zheng, J. Rossmeisl, W. Liu, Adv. Energy Mater. 13 (2023) 2204257.
[49] W.C. Xu, Z.M. Zhang, C.H. Yang, K.M. Zhao, Y.C. Wang, N. Tian, Z.Y. Zhou, S.G. Sun, Electrochem. Commun. 152 (2023) 107516.
[50] H. Inada, D. Su, R.F. Egerton, M. Konno, L. Wu, J. Ciston, J. Wall, Y. Zhu, Ultramicroscopy 111 (2011) 865–876.
[51] B. He, X. Tao, L. Li, X. Liu, L. Chen, Nano Lett. 23 (2023) 10367–10373.
[52] F. Yang, J. Ye, L. Gao, J. Yu, Z. Yang, Y. Lu, C. Ma, Y.J. Zeng, H. Huang, Adv. Energy Mater. 13 (2023) 2301408.